Structural Engineering and Mechanics, Vol. 46, No. 1 (2013) 53-73
DOI: http://dx.doi.org/10.12989/sem.2013.46.1.053

Integral Abutment Bridge behavior under uncertain thermal and time-dependent load

WooSeok Kim*[1] and Jeffrey A. Laman[2a]

[1]*Civil Engineering, Chungnam National University, Daejeon 305-764, Korea*
[2]*Civil and Environmental Engineering, Pennsylvania State University, University Park, PA 16801, U.S.A.*

(Received July 5, 2012, Revised January 14, 2013, Accepted March 6, 2013)

Abstract. Prediction of prestressed concrete girder integral abutment bridge (IAB) load effect requires understanding of the inherent uncertainties as it relates to thermal loading, time-dependent effects, bridge material properties and soil properties. In addition, complex inelastic and hysteretic behavior must be considered over an extended, 75-year bridge life. The present study establishes IAB displacement and internal force statistics based on available material property and soil property statistical models and Monte Carlo simulations. Numerical models within the simulation were developed to evaluate the 75-year bridge displacements and internal forces based on 2D numerical models that were calibrated against four field monitored IABs. The considered input uncertainties include both resistance and load variables. Material variables are: (1) concrete elastic modulus; (2) backfill stiffness; and (3) lateral pile soil stiffness. Thermal, time dependent, and soil loading variables are: (1) superstructure temperature fluctuation; (2) superstructure concrete thermal expansion coefficient; (3) superstructure temperature gradient; (4) concrete creep and shrinkage; (5) bridge construction timeline; and (6) backfill pressure on backwall and abutment. IAB displacement and internal force statistics were established for: (1) bridge axial force; (2) bridge bending moment; (3) pile lateral force; (4) pile moment; (5) pile head/abutment displacement; (6) compressive stress at the top fiber at the mid-span of the exterior span; and (7) tensile stress at the bottom fiber at the mid-span of the exterior span. These established IAB displacement and internal force statistics provide a basis for future reliability-based design criteria development.

Keywords: integral Abutment; bridge; uncertainty; load model; Monte Carlo

1. Introduction

For several decades, the finite element method has primarily been used to analyze complex structures. Despite a long history and success of FEM in many engineering fields, there are unsolved issues and continuous challenges must still be met. In order to predict the displacements and internal forces of prestressed concrete girder integral abutment bridges (IABs) under thermal load, the material and loading uncertainties must be considered. Current bridge design specifications do not establish separate thermal load factors for conventional, jointed bridges and IABs, however, behavior of the two bridge types and the consequences of the thermal loading and

*Corresponding author, Assistant Professor, E-mail: wooseok@cnu.ac.kr
[a]Professor, E-mail: JAL17@engr.psu.edu

time-dependent effects are much different.

Moreover, no studies have been conducted to understand thermal loading and time-dependent effect uncertainties and the corresponding statistics. Therefore, the present study performed an extensive Monte Carlo simulation (MCS) to establish IAB long-term displacement and internal force statistics resulting from thermal load, time-dependent effects and external soil forces. An MCS requires that thermal load and material property statistics be established and suitable numerical models be developed. Thermal load and material property input variable statistics are defined in terms of distribution type, mean and standard deviation. Bridge response over an extended time period are not currently available therefore, the present study utilizes numerical analysis to generate this long-term response.

The adoption of the idealized numerical models may introduce limited model uncertainty that is not directly evaluated in this study. However, these models were previously developed (Kim 2008, Kim and Laman 2010a, b) and were extensively calibrated and validated against 7-year field monitoring results of four IABs (Kim and Laman 2012), significantly reducing the model uncertainty. Generally, an MCS is applied to problems with complex and multiple uncertainties, which is the case presented for IAB behavior prediction. Uncertainties in several input variables cannot be avoided due to the variability, vagueness and randomness in both thermal load and material properties. Therefore, a simulation is required to examine the uncertainties of bridge displacement and internal forces.

MCS input random variables (RVs) are identified as randomly generated input variables (RGIVs) that are generated by the MCS and accepted by the numerical model to compute randomly generated output variables (RGOVs). The RGIVs include both time invariant (TI) random variables and time-varying (TV) random variables. The sets of RGIVs and RGOVs are characterized by distribution type, mean and standard deviation.

2. Scope and objectives

The primary objectives of this study are: (1) establish IAB thermal displacement and internal force statistics; (2) develop a numerical simulation model; and (3) establish IAB displacement and internal force statistics. Considered TI random variables are the material properties of the bridge components and backfill and soil strata properties. IABs included four or five prestressed concrete girders are used for short-to-medium length bridges (18 to 122 m) with 11 HP310×110 piles in a weak-axis orientation (piles bend about weak axis under longitudinal bridge movement) under 4.6 m high wall-type integral abutments. To limit the wide range of potential soil layer characterization, pile-soil lateral stiffness distribution curves within practical and commonly observed ranges were adopted.

Considered TV random variables are thermal loading of ambient temperature fluctuation, temperature gradient in the superstructure and time-dependent effects in prestressed concrete girders. The thermal loading for the analysis was limited to that representative of the northern, Mid-West and Mid-Atlantic areas of the United States where four distinct seasons are experienced. Analysis of other regions could employ the proposed procedure presented herein with available local temperature statistical information. Time-dependent effects were evaluated using the ACI 209 method.

To determine the distribution and statistics for 75-year deflections and internal forces, the MCS utilized a previously developed numerical model (Kim 2008, Kim and Laman 2010a, b) that

provides both prediction accuracy and reduction of model complexity. This nonlinear model ran 3,900 loading steps for each cycle of the MCS considering 7-day average temperature steps over a 75-year bridge life.

Adopting the Latin hypercube sampling (LHS) method reduced the number of simulations—LHS partitions the range of input variables into a desired number of strata with an equal probability and randomly draws an RGIV within each stratum. RGIVs were separated into resistance variables and load variables. The MCS considered three deterministic bridge lengths: 18.3 m (60 ft), 61.0 m (200 ft) and 122.0 m (400 ft). The following sections first establish statistics of input variables and then the MCS is implemented to establish statistics of output variables.

3. Numerical model

2D numerical models were employed for the analysis. The 2D IAB model is based on extensive validation efforts through refined 3D models (Pugasap *et al*. 2009), a field monitoring program (Laman *et al*. 2003, Laman *et al*. 2006, Laman and Kim 2009) and a calibration effort (Kim 2008, Kim and Laman 2010a). Bridge members are modeled using beam elements based on the cross sectional properties as shown in Fig. 1. The 2D numerical model includes soil-structure interaction, modeled using a condensed pile model with a lateral, nonlinear spring and a rotational spring. Abutment-to-backwall construction joint is modeled as the typical, low-reinforcement, joint using elements based on moment-curvature properties (Pugasap *et al*. 2009). Backfill-abutment interaction is modeled based on Rankine's passive and active theory.

4. Material variables

Bridge material properties and soil properties that are TI random variables also present a number of uncertainties. The present study recognizes that concrete and soil engineering property variability dominates all other uncertainties. Material property variables are: (1) concrete elastic modulus; (2) backfill stiffness; and (3) lateral pile-soil stiffness. The concrete superstructure provides resistance against vertical and longitudinal loads; backfill provides longitudinal restraint during bridge expansion; and soil layers under abutments adjacent to piles provide resistance against both bridge expansion and contraction. Each resistance variable is discussed in the following sections.

4.1 Concrete elastic modulus (E_c)

Because the specification of high strength concrete ($f_c' \geq$ 55.2 MPa (8 ksi)) has become common [4, 29, 33], a 28-day concrete compressive strength, f_c' = 55.2MPa (8 ksi) is the adopted baseline for prestressed concrete girder material. Previous research [15, 28, 33, 39] determined the statistics for normal strength concrete (20.7 MPa (3 ksi) $\leq f_c' \leq$ 34.5 MPa (5 ksi)): bias factor (λ) = 0.95 to 1.08, and coefficient of variation (COV) = 0.15 to 0.18. However, similar statistics for high strength concrete have not been established. Because published statistics for E_c are not as extensive as f_c' data, empirical equations to represent the relationship between f_c' and E_c are utilized. Three empirical equations relating f_c' to E_c are compared to available testing data. AASHTO LRFD (2010) provides the familiar empirical equation

$$E_c = 0.043 w_c^{1.5} \sqrt{f_c'} \qquad \text{(kg/m}^3\text{ and MPa)}$$
$$E_c = 33{,}000 w_c^{1.5} \sqrt{f_c'} \qquad \text{(kcf and ksi)} \tag{1}$$

ACI 363 (1998) suggests an empirical equation for high strength concrete

$$E_c = \left(w_c / 86 \right)^{1.5} \left(6900 + 3320 \sqrt{f_c'} \right) \qquad \text{(kg/m}^3\text{ and MPa)}$$
$$E_c = \left(w_c / 0.145 \right)^{1.5} \left(1000 + 1265 \sqrt{f_c'} \right) \qquad \text{(kcf and ksi)} \tag{2}$$

NCHRP18-07 (1999) also proposes an empirical equation for high strength concrete

$$E_c = 33{,}000 K_1 K_2 \left(0.140 + \frac{f_c'}{1000} \right)^{1.5} \sqrt{f_c'} \qquad \text{(ksi)} \tag{3}$$

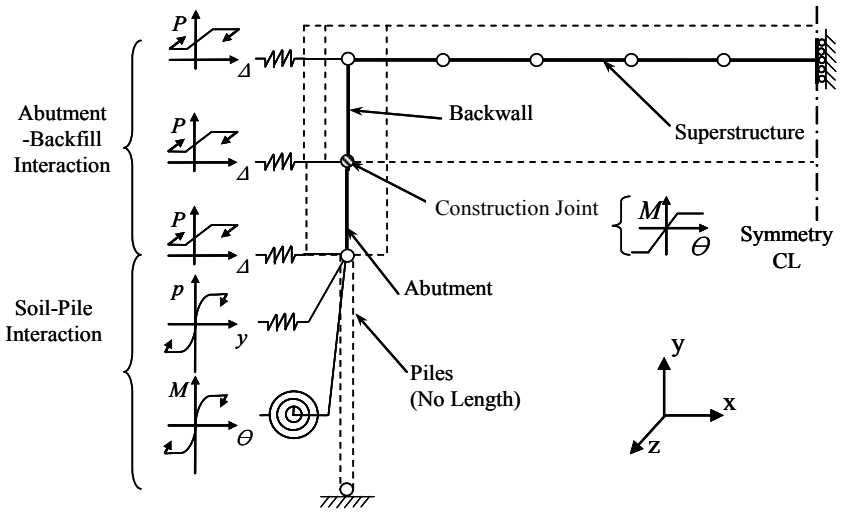

(a) Schematic of 2D numerical model

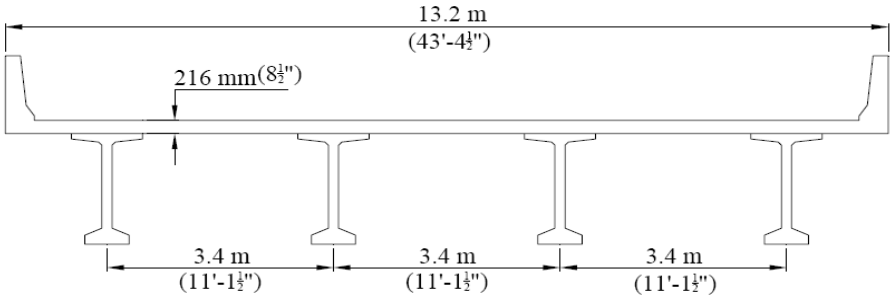

(b) Bridge cross section

Fig. 1 (a) Schematic of 2D numerical model and (b) Bridge cross-section

where K_1 and K_2 are correction factors. K_1 = 1.0 corresponds to average compressive strength. K_2 is based on the 90th percentile upper bound and the 10th percentile lower bound. A comparison of results from Eqs. (1)-(3) to 245 data points from published experiments (Laman and Kim 2009, NCHRP 18-17 1999, Rusell *et al*. 2006] appears in Fig. 2. The experimental f_c' data ranges from 55.8 to 70.3 MPa (8.1 and 10.2 ksi) which is between -11% and 12% of the mean strength ($\mu_{fc'}$). E_c varies from 23.8 to 74.4 GPa (3,450 and 10,785 ksi), which is between -39% and 90% of the mean elastic modulus (μ_{Ec}). Based on a comparison, Eqs. (1) and (3) are the most accurate for a specified f_c' = 55.2 MPa (8 ksi). 77% of E_c experimental data and 80% of f_c' data fall within two standard deviations ($\mu_{Ec} + \sigma_{Ec} \le E_c \le \mu_{Ec} - \sigma_{Ec}$, and $\mu_{fc'} + \sigma_{fc'} \le f_c' \le \mu_{fc'} - \sigma_{fc'}$) of the mean values. Collected E_c for f_c' = 55.2MPa (8 ksi) from other sources [26, 32, 38] are tabulated in Table 1. Based on this evaluation, μ_{Ec} = 39.2 GPa (5,684 ksi) and standard deviation = 7.8 GPa (1,130 ksi) for E_c are adopted in for the present study.

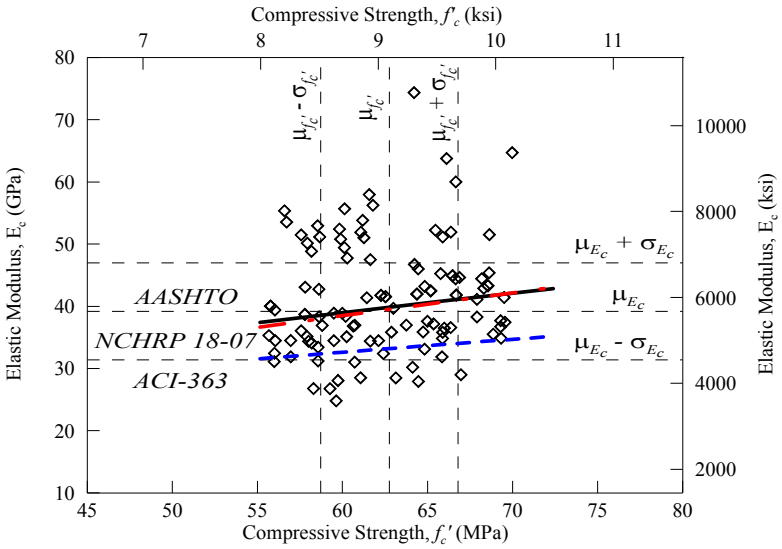

$\mu_{fc'}$ and μ_{Ec} = mean of f_c' and E_c; σ_{Ec} and $\sigma_{fc'}$ = standard deviation of f_c' and E_c

Fig. 2 Concrete elastic modulus (E_c) vs. concrete compressive strength (f_c')

Table 1 Published concrete elastic modulus, E_c statistics

Source	Concrete Elastic Modulus (E_c), f_c' = 55.2MPa (8 ksi) GPa (ksi)			
	Lower Limit	Mean	Upper Limit	Standard Deviation
Laman and Kim (2009) (Based on Eq. (1))	36.1 (5242)	38.3 (5553)	39.9 (5789)	0.9 (124)
NCHRP18-07 (1999)	23.8 (3450)	**39.2 (5684)**	74.4 (10785)	**7.8 (1130)**
Nowak and Szerszen (2003) (Based on Eq. (1))	-	37.1 (5386)	-	11.1 (1615)
Russell *et al.* (2006)	36.9 (5350)	40.2 (5830)	43.5 (6310)	-

4.2 Backfill stiffness

Abutment backfill resists longitudinal bridge expansion, however, the backfill pressure resulting from expansion is also a load on the abutments, therefore the characterization of the material is needed. Abutment backfill is generally a compacted aggregate or crushed stone that has very consistent properties across bridge construction sites. Based on an examination and evaluation of the published literature, summarized in Table 2, the mean backfill parameter values of γ_{soil} and ϕ_f are 5.7 kPa (119 pcf) and 34º with γ_{soil} and ϕ_f COVs equal to 3% and 10%, respectively [7, 11, 12, 13, 16].

There is very little published information regarding the statistics for backfill subgrade modulus, K_h. Therefore, field measurements by Laman *et al.* (2006) and Laman and Kim (2009) are utilized herein to determine the mean K_h = 12 MN/m^3 (43.8 pci). In addition, a K_h COV equal to 50% has been reported by Baecher and Christian (2003).

Table 2 Statistics for backfill soils

Source	Soil Property	COV (%)
Baecher and Christian (2003), Harr (1987), Kulhawy (1992)	Unit Weight (γ_{soil})	3 – 7
Baecher and Christian (2003), Harr (1987), Kulhawy (1992)	Friction Angle (ϕ_f)	2 – 13
Baecher and Christian (2003)	Subgrade Modulus (K_h)	50

4.3 Pile soil stiffness

Based on the published literature (Baecher and Christian 2003, Das 1999, 2002, Duncan 2000, Greimann *et al*. 1986), this study determined the mean and upper and lower limits for soil density, angle of friction, undrained shear strength, elastic modulus and ε_{50} (the strain required to mobilize 50 % of the soil strength) within a practical range as presented in Table 3. Because piles are modeled as a translational and rotational spring in the present study 2D condensed model, the maximum and minimum pile soil stiffness is first computed based on the upper and lower soil property limits for each cohesive or cohesionless soil. Then the upper and lower limit for pile-soil stiffness, as presented in Fig. 3, is established based on maximum and minimum pile soil stiffness, regardless of cohesive or cohesionless soils. The mean pile soil stiffness (or translational and rotational spring stiffnesses) is determined by the upper and lower pile soil stiffness average. A normal distribution was assumed for pile soil stiffness because all soil parameters in Table 3 follow a normal distribution.

The pile soil stiffness COV is taken from Oesterle *et al.* (1998). The condensed pile model utilizes only the pile-head stiffness for translation and rotation. Therefore, the pile- soil stiffness COV is required rather than the COVs of soil properties. Oesterle *et al.* (1998) examined numerous soil types and report a COV equal to 26%, which is adopted here to compute the COV for the translational and rotational pile soil stiffness spring.

Normal distributions for both force-displacement (pile-head translational spring) and moment-rotation (pile-head rotational spring) relationships were constructed and are presented in Fig. 3. The distributions were determined based on Table 3 mean values and the 26% COV of pile soil stiffness. These distributions were truncated at the values obtained from Table 3 upper and lower limits for the MCS.

Table 3 Soil layer properties and range determination [7, 11, 12, 13, 16]

Property	Upper Limit	Mean	Lower Limit
Sand Density, kN/m^3 (pcf)	22 (142)	19 (121)	16 (100)
Clay Density, kN/m^3 (pcf)	22 (142)	19 (121)	16 (100)
Angle of Friction (Sand), Degree	42	35	28
Undrained Shear Strength (clay), kN/m^2 (psi)	193 (28)	121 (17.5)	48 (7)
Elastic Modulus (K), MN/m^3 (pci)	353 (1,300)	271 (1000)	190 (700)
ε_{50}, mm (in)	0.13 (0.005)	0.20 (0.008)	0.25 (0.01)

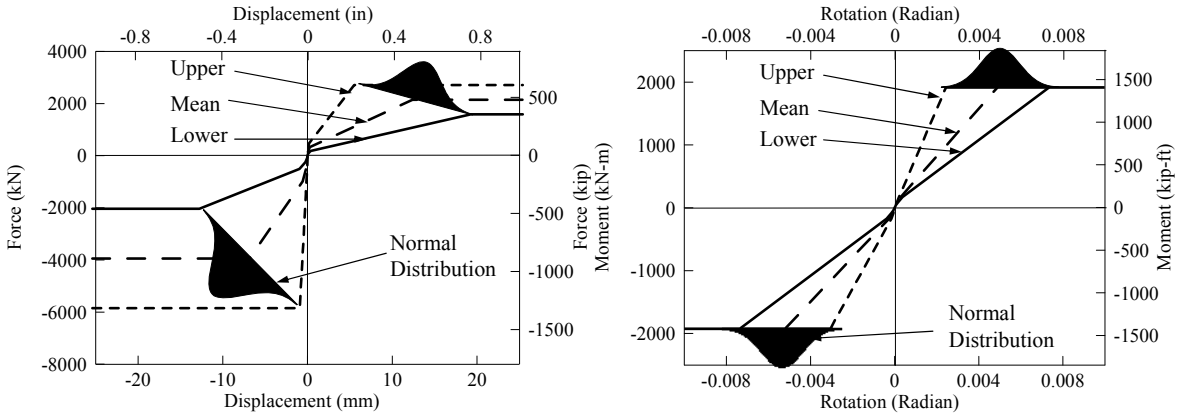

(a) Force-displacement (b) Moment-rotation

Fig. 3 Soil-pile interaction stiffness definition

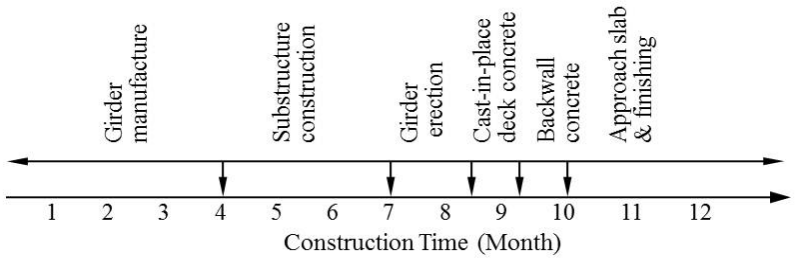

Fig. 4 Typical bridge construction timeline

5. Load variables

Load TV random variables are: superstructure temperature, thermal gradient and time-dependent effects as they are influenced by the construction timeline. Concrete thermal expansion coefficient was included as a TI random variable. Dead load and live load are not considered because analyses for dead load, traffic loads, etc. are well established elsewhere and are not the focus of the present study. Load variables are assumed to be normally distributed because the true distributions of these loads are unknown.

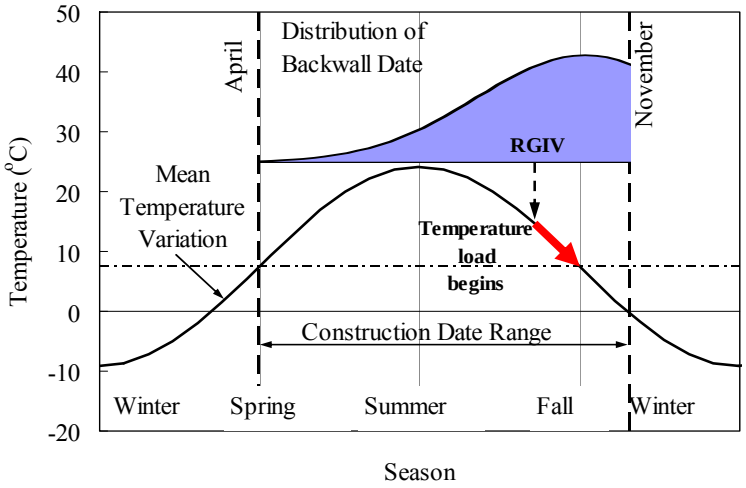

Fig. 5 Bridge temperature and backwall placement date distribution

5.1 Bridge construction timeline

The elapsed time between girder manufacture and deck and backwall placement is critical because girder concrete creep and shrinkage effects begin from manufacture. Julian date (JD) is used for the placement to be able to account for the initial bridge temperature. The bridge construction timeline in Fig. 4 is the assumed mean timeline.

A survey of bridge construction timelines by Oesterle *et al.* (1998) reports that construction begins in April and ceases in November. Construction temperature ranges from 5°C to 35°C (41°F to 95°F). Based on Fig. 5, the ambient temperature at deck and backwall placement time ranges from 5°C to 15°C (41°F to 59 °F). Also, the deck placement mean date is taken to be 100 days subsequent to girder manufacture with the standard deviation equal to 30 days, the lower limit equal to 30 days from girder manufacture, and the upper limit equal to 200 days from girder manufacture. The backwall placement date ranges from July to November, therefore, the backwall placement date mean is 242 JD (September), standard deviation is 81 days, the lower limit is 60 JD, and the upper limit is 300 JD. The backwall placement date distribution with assumed bridge temperature variation is presented in Fig. 5. Based on a RGIV backwall placement date, the initial bridge temperature in the MCS is determined and the proposed sinusoidal temperature load begins.

5.2 Superstructure temperature

Superstructure temperature is the primary loading considered in the present study, inducing longitudinal bridge displacement. Solar radiation, precipitation and wind speed all contribute to the thermal load, however, the ambient temperature has been shown to be the most directly correlated measure of bridge thermal loading (Kim and Laman 2012, Laman *et al*. 2003, Laman *et al*. 2006, Laman and Kim 2009). Three sources of historic temperature data have been used to determine the mean annual temperature, the annual mean temperature variation, i.e. temperature amplitude over a year (A in the following Eq. (4) and the standard deviation of daily temperature: a local weather station (Laman and Kim 2009), the Pennsylvania State Climatologist (PSC), and the National

Climate Data Center (NCDC) (2006). Based on the collected data the annual mean temperature, μ_T = 9.4ºC (49ºF), the daily temperature standard deviation, σ_T, is 6.5ºC (11.7ºF) and the annual mean temperature variation = 16.7ºC (30ºF). The temperature range considered in this study is similar to the cold weather region defined by AASHTO LRFD. Thermal loading of other regions can be evaluated by using the data described above. This results in the structure moving average temperature, $T_{m\,avg}$ at time t presented in Eq. (4)

$$T_{m-avg}(t) = \left[\mu_T + A\sin\left(\omega t + \phi\right)\right]$$
$$T_{m-upper\ or\ lower\ limit}(t) = \left[\mu_T + A\sin\left(\omega t + \phi\right)\right] \pm 3\left(\sigma_T\right) \tag{4}$$

where, μ_T = annual mean temperature (9.4ºC (49ºF));
A = amplitude of the seasonal temperature fluctuation (16.7ºC (30ºF));
ω = frequency (2π);
t = analysis time (year);
ϕ = phase lag, $\left(\frac{Backwall\ \ Placement\ \ Date}{365\ \ Days} - 0.09\right)$(radian),
and σ_T = standard deviation of daily temperature (6.5ºC (11.7ºF)).

ϕ equal to 0.09 adjusts the lowest temperature date to February 1. The mean daily temperature follows the sine function of Eq. 4 and is bounded by $T_{m\text{-}upper\ limit}$ and $T_{m\text{-}lower\ limit}$. At increments of seven-days, an RGIV temperature based on a normal distribution with mean = moving average temperature in Eq. 4 and a standard deviation = 6.5ºC (11.7ºF) is generated and applied as a thermal loading.

5.3 Concrete thermal expansion coefficient

A summary of published thermal expansion coefficients appears in Table 4. The study by Oesterle *et al.* (1998) considered the most extensive test data, therefore the present study has adopted 8.77 × 10^{-6}/°C (4.87 × 10^{-6}/°F) for the mean, 4.07 × 10^{-6}/°C (2.26 × 10^{-6}/°F) for lower bound and 14.4 × 10^{-6}/°C (8.0 × 10^{-6}/°F) for the upper bound and a standard deviation of 2.36 × 10^{-6}/°C (1.31 × 10^{-6}/°F).

Table 4 Statistics for concrete thermal expansion coefficient

Source	Thermal Expansion Coefficient × 10^{-6}/°C (× 10^{-6}/°F)							
	Lower Bound		Mean		Upper Bound		Standard Deviation	
AASHTO LRFD (2010, 1989)	5.4	(3.0)	10.8	(6.0)	14.4	(8.0)	-	
Emanuel and Hulsey* (1997)	-		1.00		-		0.11	
Kada *et al.* (2002)	6.5	(3.6)	-		7.6	(4.2)	-	
Oesterle *et al.* (1998)	**4.07**	**(2.26)**	**8.77**	**(4.87)**	**13.5**	**(7.49)**	**2.36**	**(1.31)**
Nilson (1991)	7.2	(4.0)	-		12.6	(7.0)	-	
Russell *et al.* (2006)	8.14	(4.52)	11.38	(6.32)	15.77	(8.76)	-	
Tanesi *et al.* (2007)	8.47	(4.71)	9.97	(5.54)	11.70	(6.50)	0.77	(0.43)
Present Study	4.07	(2.26)	8.77	(4.87)	14.4	(8.00)	2.36	(1.31)

* Normalized to the mean

5.4 Temperature gradient

Statistical data are not available for temperature gradients in concrete prestressed girders, therefore, the present study utilized the AASHTO LRFD (2010, 1989) gradient model with modifications. Because the AASHTO gradient is a design criteria, it was adopted as an upper bound. To determine a temperature gradient average and standard deviation, the AASHTO temperature gradient is divided into four regions with standard deviations by Empirical Rule (Ott and Longnecker 2001). Based on the Empirical Rule, the average is half of the AASHTO gradient and the standard deviation is a quarter of the AASHTO gradient. Along the girder depth, the temperature standard deviation is assumed to be proportional to the AASHTO gradient temperature at a given depth. The proposed temperature gradient distribution appears in Fig. 6 and temperature gradients (T_{MCS_TG}) are presented in Table 5.

5.5 Time-dependent loads

Statistics for both concrete creep and shrinkage have been determined based on published research (ACI 209 1994, Bazant and Baweja 1995, 2000, CEB-FIP 1990, Yang 2005), the results of which are presented in Table 6. The computed ACI 209 (1994) creep and shrinkage effect is taken as the mean, or expected value. The ACI 209 method of determining creep and shrinkage

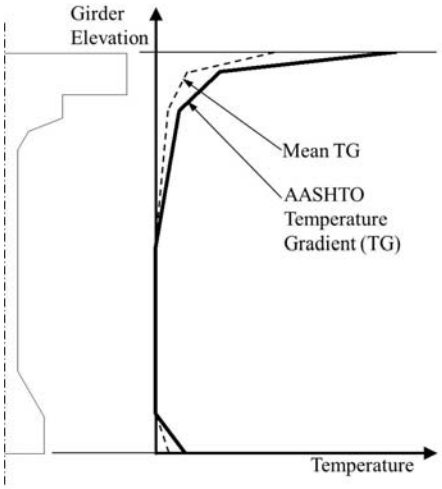

Fig. 6 RGIV Temperature gradient distribution in MCS

Table 5 Temperature gradient statistics

Bridge Length m (ft)	Gradient	Mean (μ_{TG}) °C (°F)		Standard Deviation (σ_{TG}) °C (°F)	
		Top	Bottom	Top	Bottom
18.3m (60ft)	Positive (A_{TG_P})	6.5 (11.8)	0.9 (1.7)	3.3 (5.9)	0.5 (0.9)
	Negative (A_{TG_N})	-2.9 (-5.3)	-0.6 (-1.1)	1.5 (2.7)	-0.3 (-0.6)
61.0 & 121.9m (200 & 400ft)	Positive (A_{TG_P})	4.2 (7.5)	-0.6 (-1.0)	1.0 (1..9)	-0.3 (-0.5)
	Negative (A_{TG_N})	-2.0 (-3.7)	-0.6 (-1.0)	0.5 (0.9)	-0.3 (-0.5)

predicts reasonably and accurately. ACI 209 is a simplified method that predicts material response to moisture changes, sustained loading and temperature. Basic equation with age-adjusted elastic modulus method (AEMM) is

$$\varepsilon(t) = \frac{\sigma(t_0)}{E(t_0)}\left[1+\phi(t,t_0)\right] + \frac{\sigma(t)-\sigma(t_0)}{\bar{E}(t,t_0)} + \varepsilon_{sh}(t,t_{sh,0}) \tag{5}$$

$$\bar{E}(t,t_0) = \frac{E(t_0)}{1+\chi(t,t_0)\phi(t,t_0)} \tag{6}$$

$$\phi(t,t_0) = \frac{(t-t_0)^{0.60}}{10+(t-t_0)^{0.60}}(2.35\gamma_c) \tag{7}$$

where

$\varepsilon(t)$ = total concrete strain at analysis time t,
$\sigma(t_0)$ = initial stress at the initial loading time t_0,
$E(t_0)$ = initial elastic modulus of concrete,
$\phi(t,t_0)$ = creep coefficient at the end of the time interval (t,t_0),
$\bar{E}(t,t_0)$ = age-adjusted effective elastic modulus of concrete at the end of the time interval (t,t_0),
$\varepsilon_{sh}(t,t_{sh,0})$ = shrinkage strain at the end of the time interval $(t,t_{sh,0})$,
$\chi(t,t_0)$ = aging coefficient at the end of the time interval (t,t_0), and
γ_c = correction factor.

This ACI 209 computed mean is associated with a normal distribution through a transforming multiplier function where RGIVs are generated with the mean of the transforming distribution is 1.0 and the standard deviation is 0.5. To limit the distribution to a practical range, the transforming distribution is truncated at 0.1 to prevent unrealistic magnitudes of strain, such as tensile concrete creep and shrinkage.

6. Monte Carlo simulation

Based on the previously established resistance and load variables statistics, input variables were randomly generated and accepted by the numerical model to complete an MCS. For each trial, the numerical model was solved for a 75-year bridge life based on one set of RGIVs. The solution of each simulation produces one set of RGOVs. Ultimately, the accumulated simulation data permits the determination of the listed displacement and internal force statistics. Because of the large size

Table 6 Normalized creep and shrinkage statistics

Source	Creep		Shrinkage	
	Mean	Standard Deviation	Mean	Standard Deviation
ACI 209 (1994)	1.00	0.32	1.00	0.55
Bazănt and Baweja (2000)	1.00	0.528	1.00	0.553
CEB-FIP (1990)	1.00	0.339	1.00	0.451
Yang (2005)	1.00	0.517	1.00	0.542

Note: all values presented herein are normalized to 1.0.

of the simulation, a LHS reduction technique was required to make the simulation manageable. LHS divides the input variable total range into intervals with an equal probability. Randomly selected input variables from each interval are combined, which prevents each randomly selected value from being selected more than twice. For seed values used to generate random numbers, the present study used continuous updating seed values as the random number generator to calculate the subsequent random number. This study performed 500 simulations for each bridge length based on a numerical stability study.

7. Monte Carlo simulation results

Critical 75-year bridge life displacement and internal force have been evaluated and statistics established. Each distribution for displacements and internal forces has been determined based on goodness-of-fit tests. *Kolmogorov-Smirnov* and *Anderson-Darling* goodness-of-fit tests were conducted to evaluate the statistics and a best-fit distribution considering all possible distribution types. However, the best-fit distributions obtained through this process for RGOVs, particularly distributions for L = 121.9m (400 ft), do not fully describe the peak frequency and maximum displacement and internal forces. Distribution types for RGOVs were, therefore, determined on the basis of requiring maximum values to be located within a 95% confidence interval (CI) resulting in the proposed CDF and PDF. All IAB displacements and internal forces were fit using three distribution types: normal (ND), lognormal (LND), and Weibull (WBD) distributions. In this study, each RGOV is described by distribution type, bias factor (mean to nominal ratio, λ) and COV. Table 7 presents a summary of bridge responses statistics.

7.1 Bridge axial force

A best-fit normal distribution was determined for both bridge compressive (negative) (Figs. 7(a), (b) and (c)) and tensile (positive) axial force (Figs. 7(d), (e) and (f)) with respect to L = 18.3, 61.0 and 121.9 m (60, 200 and 400 ft). The mean compressive axial force for L = 18.3, 61.0 and 121.9 m (60, 200 and 400 ft) are 2,827, 5,224 and 6,070 kN (636, 1,174 and 1,365 kips), respectively. The compressive axial force standard deviations for L = 18.3, 61.0 and 121.9 m (60, 200 and 400 ft) are 324, 891 and 795 kN (73, 200, 179 kips), respectively.

No tension forces were generated for L = 18.3 m (60 ft). For L = 61.0 m (200 ft), both tensile and compressive axial forces were generated. And for L = 121.9 m (400 ft) only tensile axial forces were generated.

7.2 Bridge bending moment

Figs. 8(a), (b) and (c) represent maximum bridge positive moments and Figs. 8(d), (e) and (f) represent maximum bridge negative moments. Bridges rarely experience positive moments in the end span and bridges with L = 18.3 m (60 ft) experience only negative moments.

Maximum negative bridge end span moments for L = 18.3 and 121.9 m (60 and 400 ft) (Figs. 8(d) and (f)) are not within a 95% CI because the load effect is significantly skewed past 8,000 (5,900 ft-kips) and 13,000 (9,600 ft-kips). These skewed results are related to soil-pile interaction curve definitions. After soil-pile interaction springs reach yield, the bridges gain no more increase in bridge moment. The proposed normal PDF for L = 61.0 m (200 ft) in Fig. 8(e) represents the

Table 7 Statistics for IAB displacements and internal forces

	Bridge Length m (ft)	Force	Distribution Type	Nominal kN (kip)	Mean kN (kip)	Bias Factor (λ)	Coefficient of Variation (COV)
Bridge Axial Force	18.3	C (-)	Normal	-1581 (-355)	-2827 (-636)	1.788	0.115
	(60)	T (+)	Normal	-546 (-123)	-869 (-195)	1.591	0.330
	61.0	C	Normal	-3225 (-725)	-5224 (-1174)	1.620	0.171
	(200)	T	Normal	137 (31)	161 (36)	1.175	1.789
	121.9	C	Normal	-4932 (-1109)	-6070 (-1365)	1.231	0.131
	(400)	T	Normal	1111 (250)	1450 (326)	1.305	0.214
Bridge Bending Moment	18.3	P (+)	Normal	-764 (-563)	-776 (-565)	1.016	0.179
	(60)	N (-)	Weibull	3115 (2297)	7880 (5812)	2.530	0.064
	61.0	P	Normal	-1005 (-741)	-1859 (-1371)	1.850	0.319
	(200)	N	Weibull	6814 (5026)	12354 (9111)	1.813	0.124
	121.9	P	Normal	-766 (-565)	-1472 (-1086)	1.922	0.396
	(400)	N	Weibull	10686 (7882)	13632 (10054)	1.276	0.097
Maximum Pile Lateral Force	18.3 (60)		Normal	1260 (283)	931 (209)	0.739	0.163
	61.0 (200)		Normal	1809 (407)	1279 (288)	0.707	0.216
	121.9 (400)		Weibull	2226 (500)	2142 (482)	0.962	0.143
Maximum Pile Moment	18.3 (60)		Normal	604 (445)	524 (386)	0.867	0.265
	61.0 (200)		Normal	1103 (814)	1268 (935)	1.150	0.354
	121.9 (400)		Normal	1559 (1150)	1843 (1359)	1.182	0.261
Maximum Pile Head Displacement	18.3 (60)		Lognormal	2.6 (0.10)	5.5 (0.218)	2.131	0.233
	61.0 (200)		Normal	8.7 (0.34)	15.3 (0.602)	1.757	0.226
	121.9 (400)		Normal	17.4 (0.69)	36.2 (1.425)	2.080	0.381
Maximum Top and Bottom Fiber Compressive and Tensile Stress	18.3	C	Normal	-471 (-0.068)	-827 (-0.120)	1.756	0.115
	(60)	T	Normal	-221 (-32.1)	-227 (-32.9)	1.027	0.377
	61.0	C	Normal	-860 (-0.125)	-1083 (-0.157)	1.259	0.204
	(200)	T	Normal	62 (8.99)	24 (3.5)	0.387	3.440
	121.9	C	Normal	-1216 (-0.176)	-1310 (-0.190)	1.077	0.160
	(400)	T	Normal	225 (32.6)	420 (60.9)	1.867	0.174

MCS simulation results. For L = 18.3 and 121.9 m (60 and 400 ft), a best-fit distribution determined did not represent maximum load effects and peak frequency well because the skewed results were not considered. A distribution model that represents maximum load effects beyond a mean value from all sample data, the proposed distribution was adjusted. It was determined that a Weibull distribution reasonably predicts the maximum load effects and is located within a 95% CI.

7.3 Pile lateral force

The lateral pile force PDFs for L = 18.3 and 61.0 m (60 and 200 ft) are normally distributed and for L = 121.9 m (400 ft) a Weibull distribution has been assumed. Fig. 9 presents pile lateral force histograms and PDFs with respect to L = 18.3, 61.0 and 121.9 m (60, 200 and 400 ft).

7.4 Pile moment

The mean pile moments for L = 18.3, 61.0 and 121.9 m (60, 200 and 400 ft) are 524, 1,268 and 1,843 kN-m (386, 935 and 1,359 ft-kips), respectively (see Fig. 10). Standard deviations are 139, 448, 481 kN-m (102, 330 and 353 ft-kips) for L = 18.3, 61.0 and 121.9 m (60, 200 and 400 ft). All proposed distributions for L = 18.3, 61.0 and 121.9 m (60, 200 and 400 ft) represent peak and maximum pile moments of histograms by MCS.

7.5 Pile head displacement

Maximum pile head displacements for L = 18.3 (60 ft) are taken to be lognormally distributed and maximum pile head/abutment displacements for L = 61.0 and 121.9 m (200 and 400 ft) are assumed to be normally distributed (see Fig. 11).

Bridge lengths 18.3 m and 61.0 m (60 and 200 ft) exhibit peak displacement of 15 mm and 35 mm (0.59 and 1.38 in), both of which can be observed for 121.9 m (400 ft). The source of these peaks originates from pile yielding. If pile soil stiffness is large and thermal movement is small, the pile head displacement falls into the smaller peak. If pile soil stiffness small, the pile may yield due to a long bridge length and larger thermal movements.

7.6 Maximum stress at the girder extreme fiber

MCS derived statistics of compressive stresses (negative) at the girder top fiber of the mid-span of the exterior span and maximum tensile stresses (positive) at the bottom fiber of the mid-span of the exterior span. Distributions for maximum compressive stresses at the top fiber are presented in Figs. 12(a), (b) and (c) and distributions for maximum tensile stresses at the bottom fiber are presented in Figs. 12(d), (e) and (f).

Bridges 121.9 m (400 ft) (Figs. 11(c) and (f)), exhibit a skewed distribution due to plastic behavior. Thus, normal distributions for L = 121.9 m (400 ft) were determined so that maximum predicted load effects are located within a 95% CI of the MCS results. 99.6% of the mid-span, exterior span, bottom fiber stress (18.3 m (60 ft)) were actually compressive rather than tensile. 99.8% of the load effects for bridges with L = 121.9 m (400 ft) experienced only tensile stresses at this location.

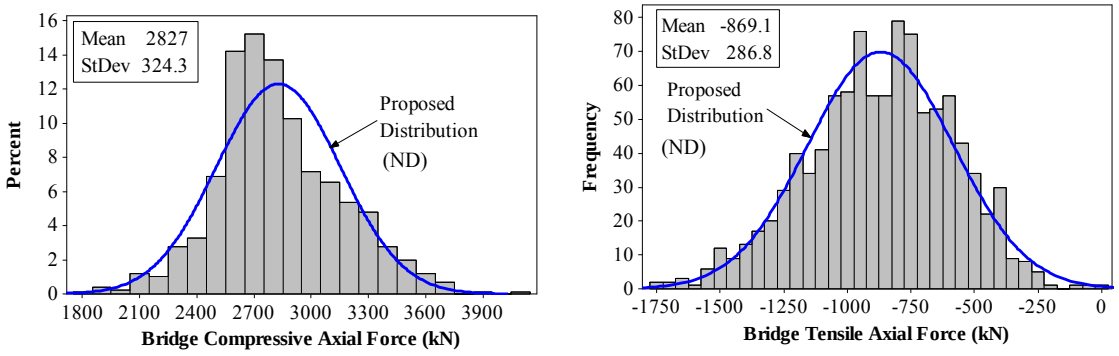

(a) L = 18.3 m (60 ft) (Compressive) (d) L = 18.3 m (60 ft) (Tensile)

Fig. 7 Histograms of bridge axial force

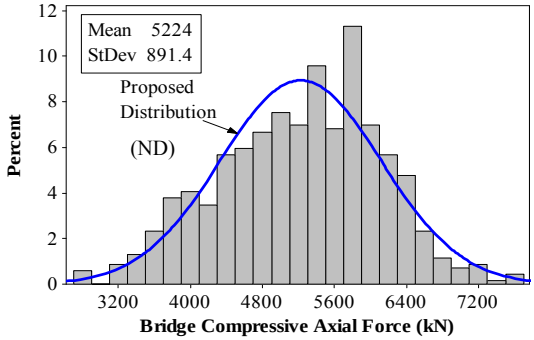

(b) L = 61.0 m (200 ft) (Compressive)

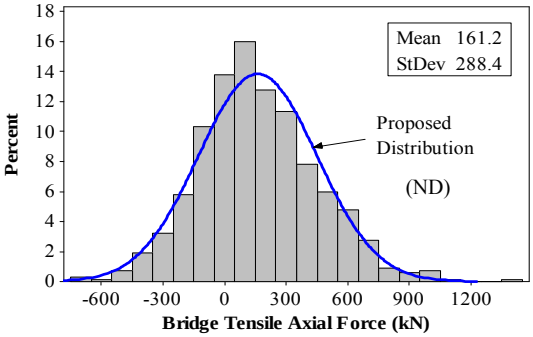

(e) L = 61.0 m (200 ft) (Tensile)

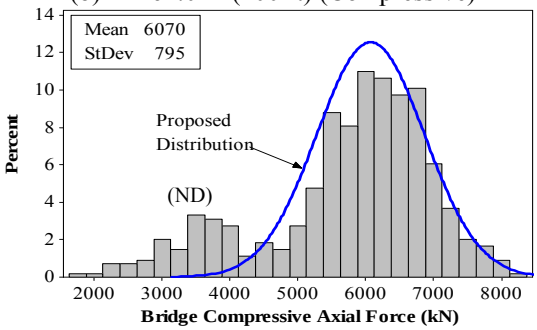

(c) L = 121.9 m (400 ft) (Compressive)

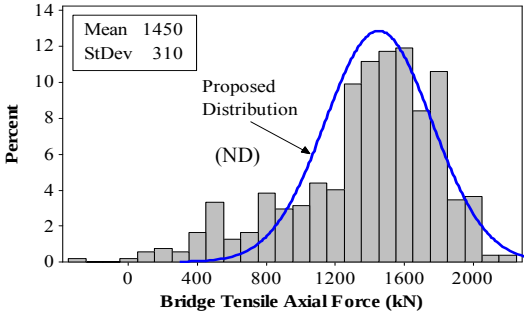

(f) L = 121.9 m (400 ft) (Tensile)

Fig. 7 Continued

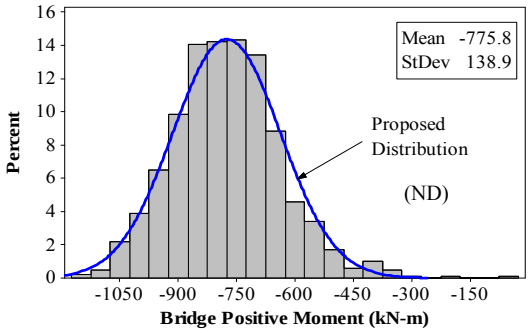

(a) L = 18.3 m (60 ft) (Positive)

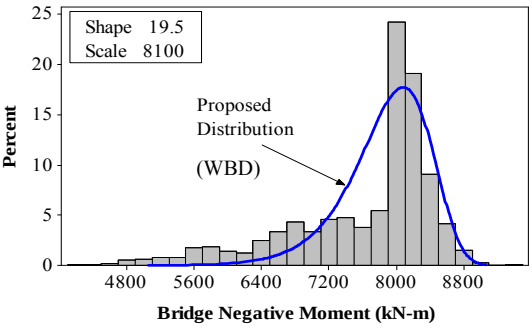

(d) L = 18.3 m (60 ft) (Negative)

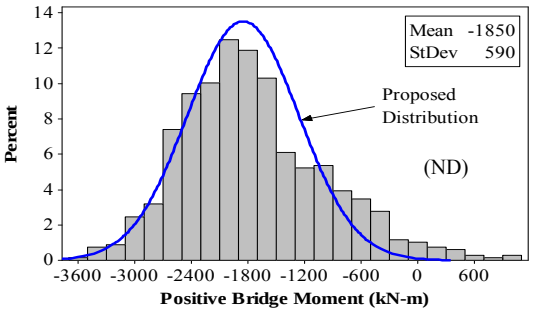

(b) L = 61.0 m (200 ft) (Positive)

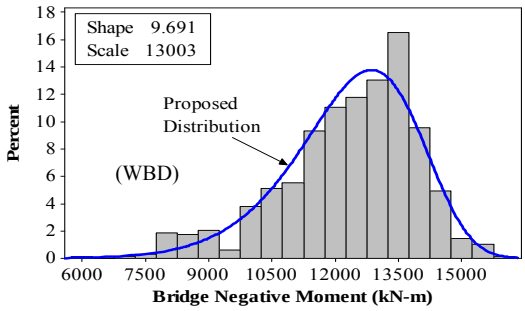

(e) L = 61.0 m (200 ft) (Negative)

Fig. 8 Histograms of maximum bridge moment

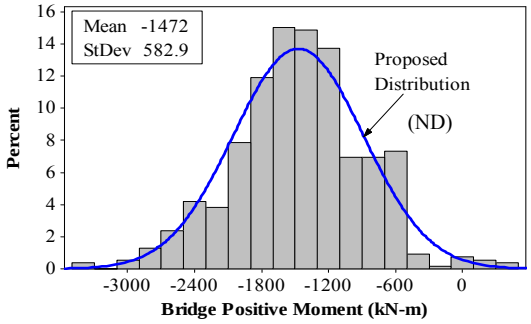

(c) L = 121.9 m (400 ft) (Positive)

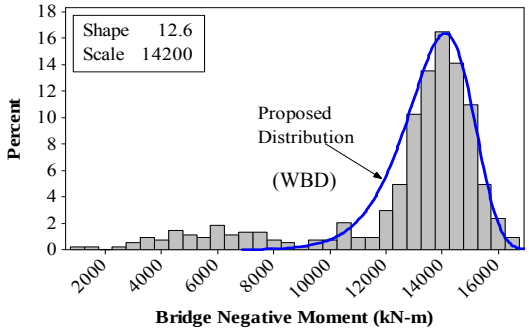

(f) L = 121.9 m (400 ft) (Negative)

Fig. 8 Continued

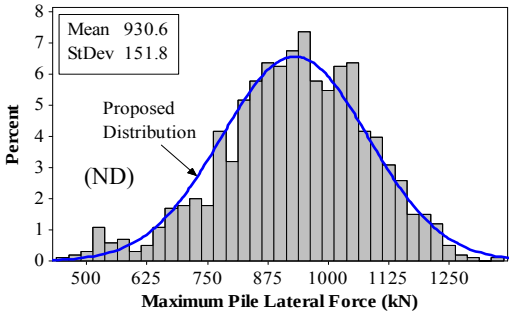

(a) L = 18.3 m (60 ft)

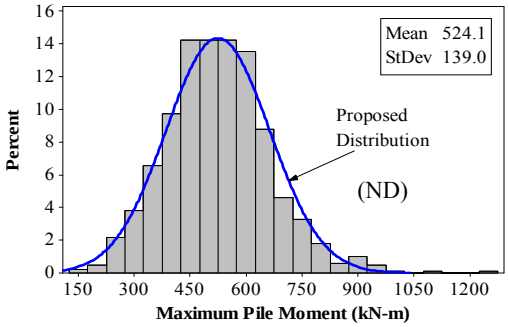

(a) L = 18.3 m (60 ft)

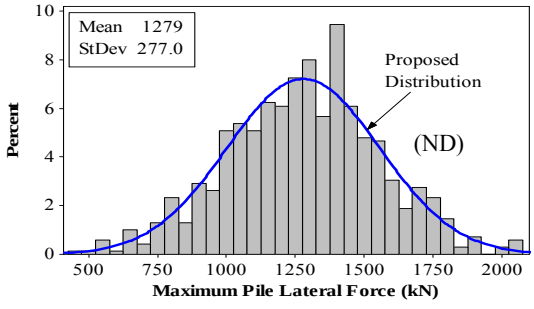

(b) L = 61.0 m (200 ft)

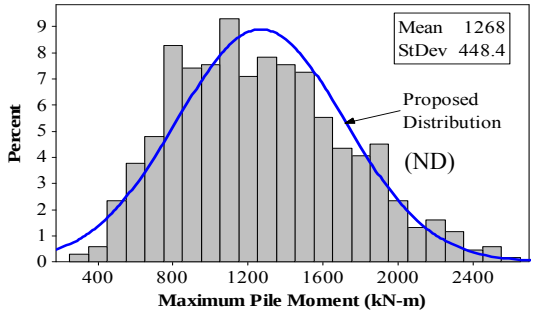

(b) L = 61.0 m (200 ft)

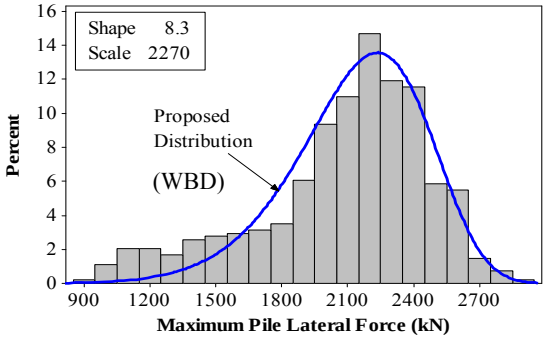

(c) L = 121.9 m (400 ft)

Fig. 9 Histograms of maximum pile lateral force

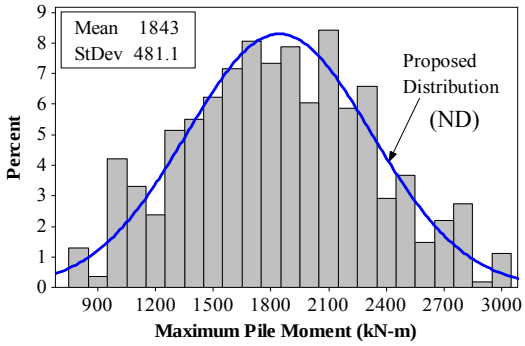

(c) L = 121.9 m (400 ft)

Fig. 10 Histograms of maximum pile moment

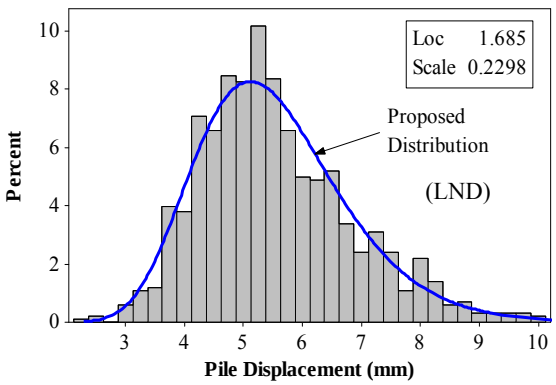

(a) L = 18.3 m (60 ft)

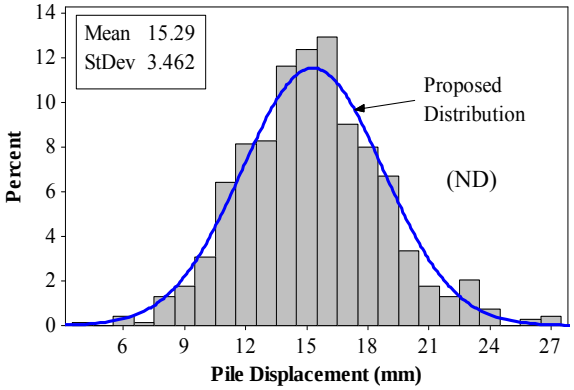

(b) L = 61.0 m (200 ft)

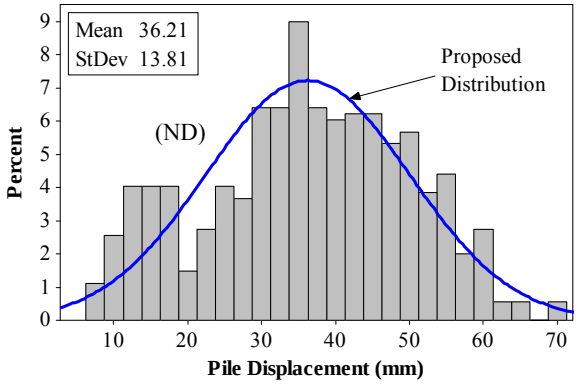

(c) L = 121.9 m (400 ft)

Fig. 11 Histograms of maximum pile head displacement

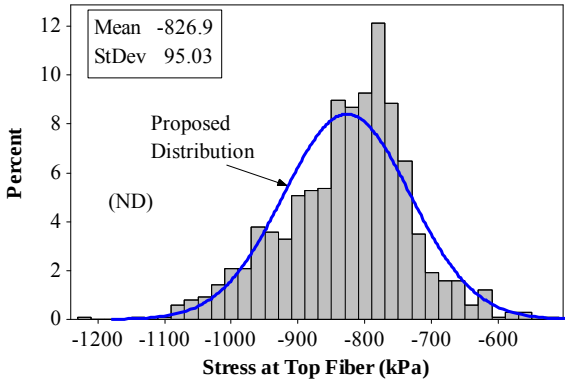

(a) L = 18.3 m (60 ft) (Compressive at the Top Fiber)

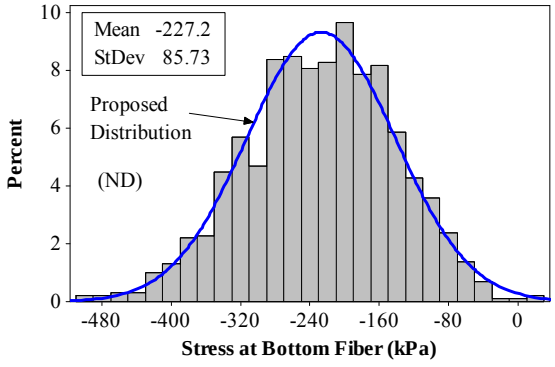

(d) L = 18.3 m (60 ft) (Tensile at the Bottom Fiber)

Fig. 12 Histograms of maximum stress at the girder extreme fiber

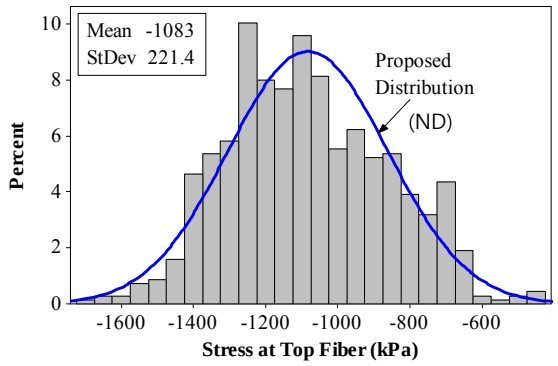

(b) L = 61.0 m (200 ft) (Compressive at the Top Fiber)

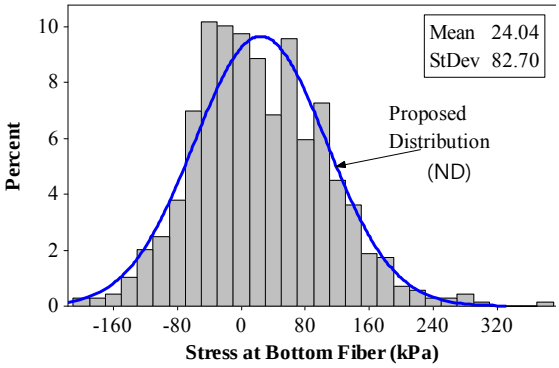

(e) L = 61.0 m (200 ft) (Tensile at the Bottom Fiber)

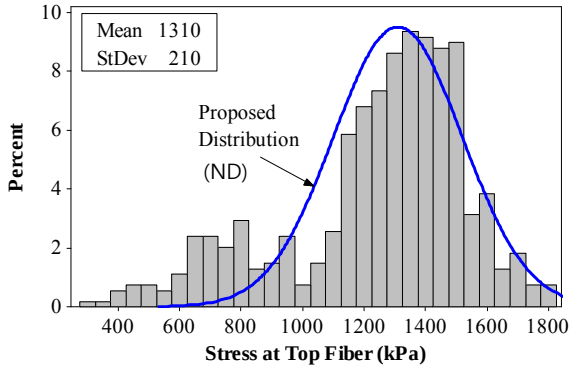

(c) L = 121.9 m (400 ft) (Compressive at the Top Fiber)

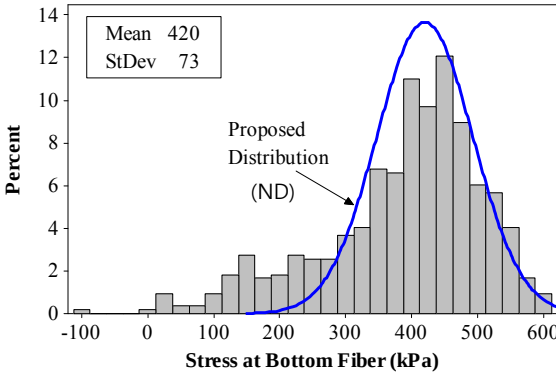

(f) L = 121.9 m (400 ft) (Tensile at the Bottom Fiber)

Fig. 12 Histograms of maximum stress at the girder extreme fiber

8. Conclusions

Although the IAB displacement and internal forces are significantly different from those of conventional bridges, uncertain thermal and time-dependent load effects are typically not considered in practice. Hence, this study extensively investigated uncertainties in IABs through simulation methods. Based on established load and resistance variable statistics, an MCS was performed utilizing the previously developed numerical model. The MCS produced data for evaluation of uncertainties in IAB load effect prediction. This data was processed to establish specific load effect statistics of interest. Resistance variables are: (1) concrete elastic modulus; (2) backfill stiffness; and (3) lateral pile soil stiffness. Load variables are: (1) superstructure temperature variation; (2) superstructure concrete thermal expansion coefficient; (3) superstructure temperature gradient; (4) concrete creep and shrinkage; (5) prestressing steel relaxation; (6) bridge construction sequence/timeline; and (7) backfill pressure on backwall and abutment. The simulation considered three deterministic bridge lengths: 18.3 m (60 ft), 61.0 m (200 ft) and 122.0 m (400 ft) and established statistics for the following load effects: (1) bridge axial force; (2) bridge bending moment; (3) pile lateral force; (4) pile moment; (5) pile head/abutment displacement; (6)

compressive stress at the top fiber at the mid-span of the exterior span; and (7) tensile stress at the bottom fiber at the mid-span of the exterior span. The conclusions for the study are as follows:

• Uncertainties inherent in long-term thermal loads and time-dependent effects and material properties and soil properties significantly influence IAB displacements and internal forces. Hence, these uncertainties in terms of reliability-based design should be considered in IAB design to improve design accuracy.

• Most IAB load effect can be predicted using a normal distribution. Certain load effects are described best by a lognormal distribution or Weibull distribution due to the nonlinear behavior of IABs.

• For long bridges, bridge compressive axial force, bridge negative bending moment, pile displacement and compressive stress at the top fiber experience two peaks in the load effect distribution that represent elastic and plastic pile behavior.

• A best-fit distribution for load effects was determined using accepted procedures. However, this best-fit distribution did not reflect the peak due to the bi-modal elastic and plastic behavior. A new distribution was, therefore, determined so that maximum load effects are located within a 95% CI.

• The established statistical parameters and distributions demonstrate that there is a significant influence and variation of range in thermal loading and time-dependent effects which are very different from the load effects in conventional bridges. Therefore, the current load factors used for IAB design should be revised to properly consider the load effects and their uncertainties. Determined IAB load effect statistics provide a basis to develop new load and resistance factors for IABs.

.

Acknowledgements

This research was supported by Basic Science Research Program through the National Research Foundation of Korea (NRF) funded by the Ministry of Education, Science and Technology (2012R1A1A1044378).

References

American Association of State Highway and Transportation Officials (AASHTO LRFD) (2010), *AASHTO LRFD Bridge Design Specifications*, Washington, DC.

American Association of State Highway and Transportation Officials (AASHTO Guide) (1989), *AASHTO Guide Specifications Thermal Effects in Concrete Bridge Superstructures*, Washington, DC.

American Concrete Institute Committee 209 (ACI 209) (1994), *Prediction of Creep, Shrinkage, and Temperature Effects in Concrete Structures*, ACI Manual of Concrete Practice Part I, American Concrete Institute, Farmington Hills, MI.

America Concrete Institute Committee 363 (ACI 363) (1998), *Guide to Quality Control and Testing of High-Strength Concrete*, American Concrete Institute, Farmington Hills, MI.

American Society of Heating, Refrigeration, and Air-Conditioning Engineers (ASHRAE) (1993), *Fundamentals Handbook*, American Society of Heating, Refrigeration, and Air-Conditioning Engineers, New York, NY.

Ayyub, B.M., and McCuen, R.H. (2003), *Probability, Statistics, and Reliability for Engineers and Scientists*, Chapman and Hall/CRC Press, Boca Raton, FL.

Baecher, G.B. and Christian, J.T. (2003), *Reliability and Statistics in Geotechnical Engineering*, John Wiley

& Sons, ISBN: 0-471-49833-5.
Bazănt, Z.P. and Baweja, S. (1995), "Justification and Refinement of Model B3 for concrete creep and shrinkage models—1. Statistics and sensitivity", *Materials and Structures*, **28**(181), 415-430.
Bazănt, Z.P. and Baweja, S. (2000), "Creep and shrinkage prediction model for analysis and design of concrete structures: model B3-short form", *Adam Neville Symposium: Creep and Shrinkage: Structural Design Effects*, American Concrete Institute, 85-100.
Comite Euro-Internationale du Beton (CEB) (1990), *CEB-FIP Model Code for Concrete Structures*, Buletin D'Information No. 213/214, Lausanne, Switzerland.
Das, B.M. (1999), *Principles of Foundation Engineering*, Brooks/Cole Publishing Company, 4th Ed., ISBN: 0-534-95403-0
Das, B.M. (2002), *Soil Mechanics Laboratory Manual*, 6th Ed., Oxford University Press.
Duncan, J.M. (2000), "Factors of safety and reliability in geotechnical engineering", *J Geotechnical and Geoenvironmental Engineering*, **126**(4), 307-316.
Emanuel, J.H. and Hulsey, J.L. (1997), "Prediction of the thermal coefficient of expansion of concrete", *J American Concrete Institute*, **74**(4), 149-155.
Galambos T. V., Ellingwood B., MacGreger J. G., and Cornell C. A. (1982), "Probability Based Load Criteria: Assessment of Current Design Practice", *J Structural Engineering*, **108**(ST5);959-977.
Greimann, L.F., Yang, P. and Wolde-Tinsae, A.M. (1986), "Nonlinear analysis of integral abutment bridges", *J. Structural Engineering*, **112**(10), 2263-2280.
Harr, M.E. (1987), *Reliability-based design in civil engineering*, McGraw-Hill, New York.
Kada, H., Lachemi, M., Petrov, N., Bonneau, O. and Aïtcin, P.C. (2002), "Determination of the coefficient of thermal expansion of high performance concrete from initial setting", *Materials and Structures*, **35**, 35-41.
Kim, W. (2008), "Simplified nonlinear numerical analysis method for integral abutment bridges", *Proceedings of the 2008 International Bridge Conference*, Pittsburgh, PA, IBC-08-43, 290-298.
Kim, W. and Laman, J.A. (2010a), "Numerical analysis method for long-term behavior of integral abutment bridges", *Eng. Struct.*, **32**(8), 2247-2257.
Kim, W. and Laman, J.A. (2010b), "Integral abutment bridge response under thermal loading", *Eng. Struct.*, **32**(6), 1495-1508.
Kim, W. and Laman, J.A. (2012), "7-year field monitoring of four integral abutment bridges", *J. of Performance of Constructed Facilities*, **26**(1), 54-64.
Kulhawy, F.H. (1992), "On the evaluation of soil properties", *ASCE Geotech. Special Publication*, **31**, 95-115.
Lacasse, S. and Nadim, F. (1997), "Uncertainties in characterizing soil properties", *Norwegian Geotechnical Institute*, Oslo, Norway, **201**, 49-75.
Laman, J.A., Linzell, D.G., Leighty, C.A. and Fennema, J.L. (2003), *Methodology to Predict Movement and Stresses in Integral Abutment Bridges*, Report No. FHWA-PA-2002-039-97-04(80), Pennsylvania Transportation Research Council.
Laman, J.A., Pugasap, K. and Kim, W. (2006), *Field Monitoring of Integral Abutment Bridges*, Report No. FHWA-PA-2006-006-510401-01, Pennsylvania Transportation Research Council.
Laman, J.A. and Kim, W. (2009), *Monitoring of Integral Abutment Bridges and Design Criteria Development*, Report No. FHWA-PA-2009-005-PSU002, Pennsylvania Transportation Research Council, Harrisburg, PA.
Mirza, S.A., Hatzinikolas, M. and MacGregor, J.G. (1979), "Statistical descriptions of the strength of concrete", *J. Structural Div.*, **105**(6), 1021-1037.
National Cooperative Highway Research Program (NCHRP 18-07), Tadros, M.K., Al-Omaishi, M., Seguirant, S.J. and Gallt, J.G. (1999), *Prestress Losses in Pretensioned High-Strength Concrete Bridge Girders*, Transportation Research Board, Washington, D.C., Rep 496.
National Climate Data Center (NCDC) (2006), *Comparative Climate Data for the United States through 2006*, National Oceanic and Atmospheric Administration. (http://www.noaa.gov/)
Nilson, A.H. (1991), *Design of Concrete Structures*, Eleventh Edition, McGraw-Hill Inc., New York.

Nowak, A.S. and Szerszen, M.M. (2003), "Calibration of design code for buildings (ACI 318): Part 1-statistical models for resistance", *ACI Structureal Journal*, **100**(3), 377-382.
Nowak, A.S., Yamani, A.S. and Tabsh, S.W. (1994), "Probabilistic models for resistance of concrete bridge girders", *ACI Structural Journal*, **91**(3), 269-276.
Oesterle, R.G., Refai, T.M., Volz, J.S., Scanlon, A. and Weiss, W.J. (1998), *Jointless and Integral Abutment Bridges Analytical Research and Proposed Design Procedures*, Construction Technology Laboratories, Inc., Draft Final Report to Federal Highway Administration, Washington, D.C.
Ott, R.L. and Longnecker, M. (2001), *An Introduction to Statistical Methods and Data Analysis*, 5th Edition, Duxbury, Thomson Learning, Inc., Pacific Grove, CA.
Pugasap, K., Kim, W. and Laman, J.A. (2009), "Long-term response prediction of integral abutment bridges", *J. Bridge Eng.*, **14**(2), 129-139.
The Pennsylvania State Climatologist (PSC), http://pasc.met.psu.edu/PA_Climatologist.
Russell, H.G., Miller, R.A., Ozyildirim, H.C. and Tadros, M.K. (2006), *Compilation and Evaluation of Results from High-Performance Concrete Bridge Porjects, Volume I: Final Report*, FHWA-HRT-05-056. U.S. Department of Transportation, Federal Highway Adminstration, McLean, VA.
Stewart, M.G. (1997), "Time-dependent reliability of existing RC structures", *J. Struct. Eng*., **123**(7), 896-902.
Tanesi, J., Kutay, M.E., Abbas, A. and Meininger, R. (2007), "Effect of CTE variability on concrete pavement performance as predicted using the mechanistic-empirical pavement design guide", *Proceedings: TRB 86th Annual Meeting,* Transportation Research Board, Washington D.C.
Yang, I. (2005), "Uncertainty and updating of long-term prediction of prestress forces in PSC box girder bridges", *Computers and Structures*, **83**, 2137-2149.